ACS APPLIED MATERIALS & INTERFACES

Research Article

www.acsami.org

HATCN-based Charge Recombination Layers as Effective Interconnectors for Tandem Organic Solar Cells

Rong-Bin Wang, Qian-Kun Wang, Hao-Jun Xie, Lu-Hai Xu, Steffen Duhm,* Yan-Qing Li, and Jian-Xin Tang*

Institute of Functional Nano & Soft Materials (FUNSOM), Soochow University, Suzhou 215123, China

Supporting Information

ABSTRACT: A comprehensive understanding of the energy-level alignment at the organic heterojunction interfaces is of paramount importance to optimize the performance of organic solar cells (OSCs). Here, the detailed electronic structures of organic interconnectors, consisting of cesium fluoride-doped 4,7-diphenyl-1,10-phenanthroline and hexaazatriphenylene−hexacarbonitrile (HATCN), have been investigated via in situ photoemission spectroscopy, and their impact on the charge recombination process in tandem OSCs has been identified. The experimental determination shows that the HATCN interlayer plays a significant role in the interface energetics with a dramatic decrease in the reverse built-in potential for electrons and holes from stacked subcells, which is beneficial to the charge recombination between HATCN and the adjacent layer. In accordance with the energy-level alignments, the open-circuit voltage of tandem OSC incorporating a HATCN-based interconnector is almost 2 times that of a single-cell OSC, revealing the effectiveness of the HATCN-based interconnectors in tandem organic devices.

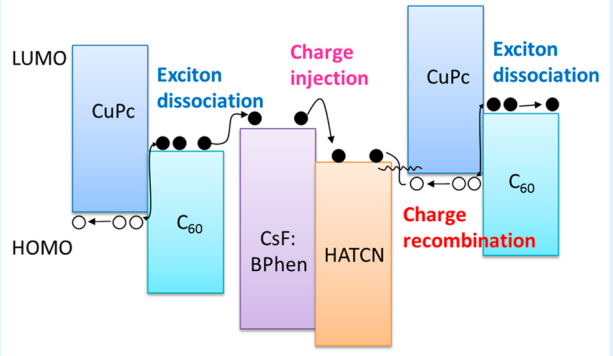

KEYWORDS: *tandem organic solar cell, interconnector, charge recombination layers, HATCN, electronic structure*

1. INTRODUCTION

Over the past few decades, organic solar cells (OSCs) have drawn more and more attention due to their low cost, ease of the fabrication, and favorable mechanical flexibility. The power conversion efficiency (PCE) of OSCs based on small molecules and polymers has been significantly improved with the development of new photovoltaic materials and novel device configurations.[1−10] For all single-junction solar cells, however, the PCE is limited to the Shockley−Queisser limit.[11] Moreover, for organic materials, a short exciton diffusion length and low charge carrier mobility lead to further low solar energy utilization ratios and huge thermodynamical loss. Generally, to capture more solar light and gain a high PCE, a useful approach is to make a tandem OSC, that is, stacking multiple junctions with complementary absorption spectra in a series connection.[2,3,12] Furthermore, the stacked structure of multijunction cells can result in an increase of the open circuit voltage (V_{OC}), due to the addition of photovoltage of each individual subcell.[13] Consequently, various efforts have been put into tandem OSCs[14−19] and the best device performance, reported up to date, is a PCE of 10.6%.[14]

Tandem OSCs are usually composed of two subcells and a sandwiched interconnector. For this stacked architecture, the interconnector plays a decisive role in the device performance and needs to satisfy the following basic requirements:[20] high transparency to reduce the optical loss, suitable interface energetics for a quasi-ohmic-contact with the adjacent layers for electron and hole injections, and the balance of charge carriers from different subcells by avoiding the formation of a reverse built-in potential. Possessing these properties will provide interconnectors with effective recombination capability as well as ohmic contacts with subcells. As a result, electrons from the bottom cell can effectively combine with holes from the top cell without any large energy loss, and thus the open-circuit voltage (V_{OC}) of tandem OSCs can be maximized for the performance improvement. In addition, the fabrication of the interconnectors in tandem OSCs should avoid high-temperature processing, which could damage the volatile layers of the bottom cell.[20]

Recently, multiple efficient intermediate layers have been developed for small-molecular tandem OSCs, including the insertion of thin metal layers (Au, Ag),[15,18,21−23] and intercalation of transition metal oxides such as vanadium oxide, tungsten oxide, and molybdenum oxide.[19,22,24−26] However, these inorganic materials usually involve the high-temperature evaporation, and the bottom layer will be inevitably damaged during the device fabrication. Hexaazatriphenylene−hexacarbonitrile (HATCN), as a strong electron acceptor with a low vacuum-deposition temperature (~200 °C),[27] has a deep-lying lowest unoccupied molecular orbital

Received: July 16, 2014
Accepted: August 20, 2014
Published: August 20, 2014

Table 1. Architectures of OSC Cells

device and units	layers
single-cell	ITO/D-A/BPhen(8 nm)/Al (100 nm)
tandem A	ITO/D-A (bottom)/CRL1/D-A (top)/BPhen (8 nm)/Al (100 nm)
tandem B	ITO/D-A (bottom)/CRL2/D-A (top)/BPhen (8 nm)/Al (100 nm)
D-A	CuPc (30 nm)/C_{60} (60 nm)
CRL1	CsF:BPhen (30 wt %, 8 nm)/HATCN (2 nm)
CRL2	CsF:BPhen(30 wt %, 8 nm)

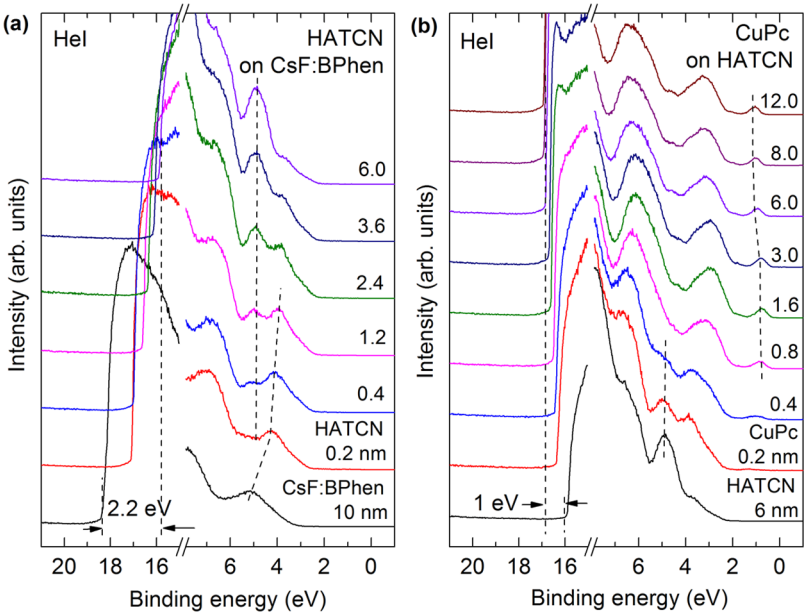

Figure 1. HeI UPS spectra of CuPc/HATCN/CsF:BPhen on the ITO substrate. (a) Incremental deposition of HATCN on CsF:BPhen. (b) Further deposition of CuPc on the HATCN/CsF:BPhen.

(LUMO) and high optical transparency in the visible spectral region.[28−30] HATCN has been widely used in organic light-emitting diodes for hole transport or the modification of hole-injection barriers,[31,32] implying that the incorporation of HATCN into interconnectors for small-molecular tandem OSCs could provide a feasible way to reduce the hole-injection barrier and effectively transport electrons. Nevertheless, only a few pertinent studies have been conducted to date,[33] while HATCN was used in combination with Ag, making the advantage of low-temperature processing obsolete.

In this study, we used the in situ X-ray and ultraviolet photoemission spectroscopies (XPS and UPS) to investigate the electronic structures of the interconnector used for tandem OSCs, which was composed of cesium fluoride doped 4,7-diphenyl-1,10-phenanthroline (CsF:BPhen, 30 wt %) and HATCN. The impact of HATCN-based charge recombination layers (CRLs) on the performance of tandem OSCs was also verified, showing that an effective interconnector could double the V_{OC} as compared to a single-cell device.[13]

2. EXPERIMENTAL DETAILS

2.1. Device Fabrication and Characterization. All OSCs were fabricated on patterned indium tin oxide (ITO)-coated glass substrates with a sheet resistance of 20 Ω per square. Prior to film evaporation, the substrates were cleaned in an ultrasonic bath successively using acetone, ethanol, and deionized water, dried in an oven, and finally exposed to UV-ozone treatment for 15 min. Then, the ITO glass substrates were transferred to a vacuum deposition chamber with a base pressure of 2×10^{-6} Torr for thermal evaporation of the organic and inorganic materials. Materials deposition rate and layers thickness were monitored with quartz-crystal monitors. The active layers consisted of copper phthalocyanine (CuPc) as the donor and fullerene (C_{60}) as the acceptor, which is a frequently used material combination in OSCs.[24,34] The CsF:BPhen mixture was formed by coevaporating two materials from two separated sources that were controlled with different quartz-crystal monitors. A shadow mask was utilized to define the cathode, resulting in a device area of 0.1 cm^2. Finally, the devices were transported into an interconnected nitrogen-filled glovebox for encapsulation with an epoxy-resin-sealed glass cap. The detailed device structures and layer thicknesses of single cell (control device) and tandem cells are shown in Table 1. To ensure the consistent results, each series of tandem and control devices were simultaneously fabricated in the same batch for the deposition of organic and metal materials. Current density−voltage (J−V) characteristics of OSCs were measured with a programmable Keithley model 2612 power source under AM 1.5 solar illumination from a Newport 150W solar simulator. Illumination intensity was measured with a calibrated Oriel radiant power meter.

2.2. Characterization of Electronic Structures. Interface characterization was carried out in a Kratos AXIS Ultra-DLD ultrahigh vacuum photoemission spectroscopy system, which includes an analysis chamber, an evaporation chamber, and a multiport carousel chamber. The base pressures in three chambers preceded 5×10^{-10}, 6×10^{-10}, and 6×10^{-10} Torr, respectively. ITO substrates were ex situ solvent cleaned and treated by UV-ozone in the same way to the device fabrication. All materials were sufficiently out-gassed before film deposition. HATCN and CuPc were in situ thermally deposited onto the substrates with a growth rate of 1−2 Å s^{-1} in the evaporation chamber. CsF and BPhen were coevaporated from two separated sources. A quartz-crystal microbalance was used to monitor the deposition rate and film thickness. After each deposition process,

samples were transferred to the analysis chamber without breaking ultrahigh vacuum for UPS and XPS measurements. UPS measurements were conducted to characterize the vacuum level (VL) and valence states by using the HeI excitation line (21.2 eV) generated from a helium discharge lamp with an instrumental energy resolution of 0.1 eV. A negative bias voltage of 10 V was applied to enable the observation of secondary electrons during UPS measurements. The interfacial chemical reaction and gradual changes of core levels were measured by XPS using a monochromatic Al Kα source (1486.6 eV) with a resolution of 0.5 eV. All the spectra were acquired at room temperature. The Au $4f_{7/2}$ peak position and the Fermi-level (E_F) edge of an Au film were used to calibrate the binding energy (BE) scale and all the UPS and XPS spectra are referred to the E_F as zero BE.

3. RESULT AND DISCUSSION

3.1. Electronic Structures of CuPc/HATCN/CsF:BPhen Layers. To get a comprehensive understanding of the role of the HATCN-based interconnectors, the electronic structures were measured by UPS and XPS. The VL shifts and the evolution of the highest occupied molecular orbitals (HOMO) can be determined by the secondary electron cutoff at high BE region and the onset at low BE region, respectively, which can be used for the determination of the energy-level alignment at the interface. Figure 1a shows thickness-dependent UPS spectra of HATCN deposited on a 10 nm thick CsF:BPhen layer on UV-ozone treated ITO glass. The bottom spectrum shows the photoemission from the CsF:BPhen layer with a 30 wt % CsF doping ratio, where the secondary electron cutoff indicates a VL value of 3.0 eV above E_F. Upon the 6 nm thick HATCN deposition, the spectral features of CsF:BPhen were gradually attenuated and progressively shifted by 1.0 eV toward a lower BE, while the VL shifts by 2.2 eV away from E_F. It is noteworthy that no new features emerge in the energy gap region by HATCN deposition, implying a physical adsorption process at the HATCN/CsF:BPhen interface. For a 6 nm thick HATCN layer, the onset of the HOMO-derived peak is located at 4.0 eV below E_F. There is almost no position change for the HOMO peak maximum (at 4.8 eV below E_F) for all HATCN coverage, indicating that HATCN exhibits flat energy level conditions during the incremental deposition process. The corresponding ionization potential (IP) value for HATCN, as determined by the energy difference between the VL position and HOMO onset, is 9.2 eV, which is similar to previously reported results.[28]

After the deposition of HATCN, CuPc was stepwise evaporated onto the superimposed layer (Figure 1b). Upon deposition of a 0.2 nm thick CuPc layer, the VL presents a shift of ~0.4 eV toward E_F (as determined from the secondary cutoff region). The HOMO derived peak for the CuPc layer exhibits its onset at 0.4 eV below E_F and exhibits successive growth of intensity, including a slight shift toward the higher BE region by increasing the CuPc thickness. The top spectrum corresponds to a 12 nm thick CuPc layer and its HOMO edge is finally located at 0.5 eV BE. The total VL shift between the 6 nm HATCN and the 12 nm CuPc layer is 1.0 eV. In addition, no gap states can be observed in Figure 1b, revealing the physisorption of CuPc on HATCN.

XPS measurements were carried out in order to monitor the chemical interactions at the interface. The lower parts of Figure 2a,b illustrate the evolution of C 1s and N 1s core levels of the HATCN/CsF:BPhen interface on the ITO substrate. For the CsF:BPhen layer, the C 1s- and N 1s-derived peaks are centered at 285.5 and 399.5 eV BE, respectively. Evaporation of 0.2 nm HATCN shifts these peaks by about 0.4 eV toward a lower BE. With increasing HATCN thickness, the intensities of C 1s and N 1s core levels contributed by CsF:BPhen are attenuated gradually and the peak positions keep on moving toward a lower BE and are finally located at 284.6 and 398.6 eV BE, respectively. Due to the different chemical environment of C and N in HATCN and CsF:BPhen, their C 1s- and N 1s-derived peaks appear at distinctively different binding energy position. The C 1s- and N 1s-derived peaks, which are assigned to HATCN (centered at 287.3 and 400.4 eV BE, respectively) gain intensity with increasing HATCN thickness without any peak position changes. These observations are in accordance with the above-mentioned UPS results. Furthermore, no new features could be observed in the core level spectra, implying the absence of a strong chemical interaction between HATCN and CsF:BPhen.

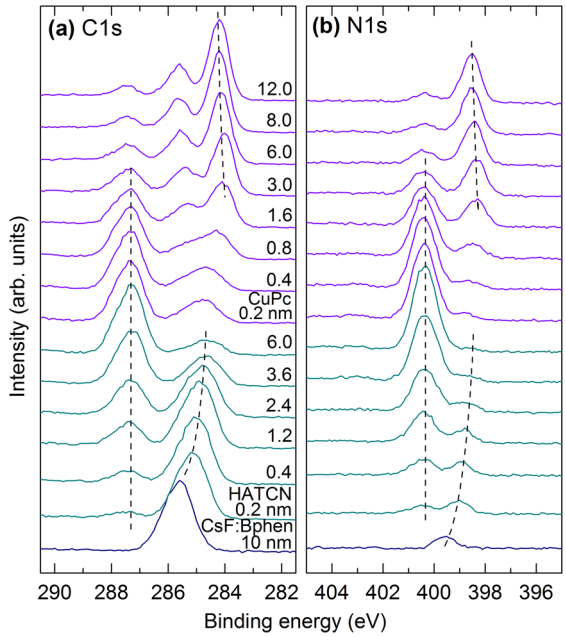

Figure 2. XPS spectra of (a) C 1s and (b) N 1s core levels obtained upon the CuPc/HATCN/CsF:BPhen trilayer construction.

The upper parts of Figure 2a,b show the XPS spectra for the CuPc/HATCN interface. With increasing CuPc thickness, all the core levels of CuPc exhibit a slight shift toward higher BE and an increase in peak intensity. These BE shifts for C 1s and N 1s core levels are consistent with the UPS results in Figure 1. There are some overlaps for C 1s between CuPc and CsF:BPhen in the low BE region, resulting in a large width of the C 1s-derived peak for the CuPc coverage lower than 1 nm thick. The three peaks for the top spectrum of 12 nm thick CuPc in Figure 2a can be assigned to aromatic carbon of the benzene rings, pyrrole carbon linked to nitrogen, and a $\pi-\pi^*$ satellite feature from the pyrrole carbon.[35]

3.2. Energy-Level Alignment of HATCN-based CRLs. The energy-level alignment diagrams of the CuPc/HATCN/CsF:BPhen trilayer interfaces and the CuPc/CsF:BPhen bilayer are shown in Figure 3 (see Figures S1 and S2 (Supporting Information) for UPS and XPS results). The transport gaps, used to obtain the LUMO position of HATCN, CuPc and BPhen are 4.2,[36] 2.3,[37] and 4.2 eV,[38] respectively (as measured by UPS and inverse photoemission spectroscopy). The interface dipole was determined by the secondary electron cutoff shift and the HOMO edges for each layer were gained from the low BE region of the spectra. Such energy-level

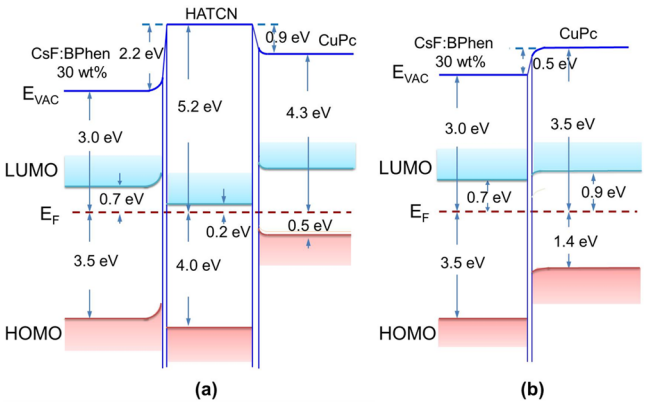

Figure 3. Schematic energy-level diagrams of (a) CuPc/HATCN/CsF:BPhen and (b) CuPc/CsF:BPhen. The HOMO positions were extracted from the UPS spectra and the LUMO positions were estimated by adding the transport gaps.

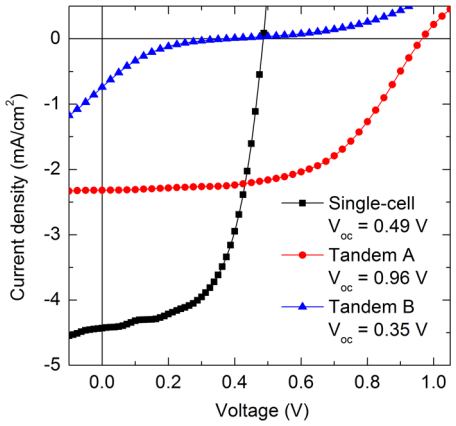

Figure 4. Current density–voltage (J–V) characteristics of a single-cell (the control device) and tandem OSCs under 100 mW cm^{-2} AM 1.5G irradiation.

diagrams can be of great help to evaluate whether a CRL is suitable for the operation of tandem OSCs. In tandem OSCs incorporating CRLs, as shown in Figure 3, illumination leads to exciton dissociation andcharge separation in two subcells, and eventually the accumulation of electrons in the CsF:BPhen's LUMO and holes in the CuPc's HOMO will occur. Except for the extractions of electrons and holes by the electrodes, the electrons and holes in the layers adjacent to the CRL need to recombine for the continuous light-to-electrical conversion in tandem OSCs.

As displayed in Figure 3, the HATCN layer has a significant influence on the energy-level alignment, due to the formation of a remarkable interface dipole between HATCN and CsF:BPhen layers (~2.2 eV). This dipole is related to the low VL of CsF:BPhen (3.0 eV) and the large electron affinity of HATCN (5.0 eV),[36] which causes a situation reminiscent Fermi-level pinning to maintain thermodynamic equilibrium.[39,40] Moreover, the interface dipole leads to an upward HOMO level shift (~1.0 eV) in the CsF:BPhen layer close to the interface. As the LUMO positions are expected to follow the HOMO shift (Figure 3a),[41] it seems to be detrimental to electron transport from CsF:BPhen to HATCN. However, if the layer with such an energy level shift only has a small thickness, the electron blocking could be overcome by quantum tunneling.[42,43] Finally, the large dipole by the incorporation of HATCN reduces the energy offset between CsF:BPhen's LUMO and CuPc's HOMO from 1.7 to 1.2 eV, and increases the energy offset between the LUMOs of CsF:BPhen and CuPc. Such a change in the energy level offset is beneficial for high charge recombination rates and thereby small reverse built-in potential. For the CRL without HATCN, the large energy gap between CsF:BPhen's LUMO and CuPc's HOMO cannot provide a smooth recombination channel, leading to a large reverse built-in voltage in the interconnector for tandem OSCs. Moreover, the small energy offset between the LUMOs of CsF:BPhen and CuPc might cause the electron diffusion from CsF:BPhen into CuPc, which is also detrimental to device performance.

3.3. Device Performance of OSCs and Discussion. To verify the above-mentioned observation, tandem OSCs based on different CRLs were fabricated, and compared with a single-cell control device. Figure 4 shows the J–V characteristics measured under simulated AM 1.5G solar illumination with an incident intensity of 100 mW cm^{-2}. The corresponding performance parameters of OSCs are summarized in Table 2.

Table 2. Parameters of the Device Performance[a]

devices	V_{OC} (V)	J_{SC} (mA·cm^{-2})	FF [%]
single-cell	0.49 (±0.02)	4.42 (±0.12)	60.0 (±0.3)
tandem A	0.96 (±0.02)	2.31 (±0.15)	57.5 (±0.2)
tandem B	0.35 (±0.03)	0.63 (±0.14)	15.1 (±0.4)

[a]The average values were obtained from eight cells.

Tandem OSCs exhibit very distinctive changes in device performance when different CRLs are used. Based on a CsF:BPhen/HATCN CRL, the tandem cell (device A) has a V_{OC} of 0.96 V, which is nearly twice that of the single cell of 0.49 V. In contrast, device B with only CsF:BPhen in the CRL shows a V_{OC} of 0.35 V, which is even lower than that of the control device. These results are consistent with the UPS measurements and confirm that the reduction of the LUMO–HOMO gap of CsF:BPhen and CuPc leads to efficient charge recombination in the CRL.

The working mechanisms of tandem OSCs with different CRLs are schematically shown in Figure 5. It can be expected that the V_{OC} of two subcells (V_{OC1} and V_{OC2}) in a tandem device equals that of the single cell

$$V_{OC1} \approx V_{OC2} \approx V_{OC}\,(\text{single cell}) = 0.49\ \text{V} \quad (1)$$

The V_{OC} of a tandem device is thus given by

$$V_{OC}\,(\text{tandem}) \approx 2V_{OC}\,(\text{single cell}) - V_{CRL} \quad (2)$$

where V_{CRL} is the reverse built-in voltage in the CRL, which is a voltage loss to the tandem device. For the HATCN-based interconnector (Figure 5a), this loss (i.e., V_{CRL1}) is virtually zero (0.02 V). For the interconnector without the HATCN layer (Figure 5b), however, the energy level mismatch between CuPc's HOMO and CsF:BPhen's LUMO results in a high voltage loss (for example, $V_{CRL2} \approx 0.63$ V), which largely obstructs the charge recombination. Moreover, the electrons can easily transport from CsF:BPhen's LUMO to CuPc's LUMO, leading to the invalidation of the top subcell.

4. CONCLUSIONS

In summary, the detailed electronic structures of HATCN-based interconnectors for tandem OSCs have been investigated

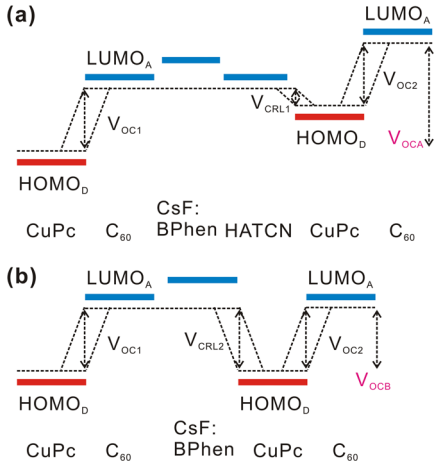

Figure 5. Schematic energy level offsets of tandem OSCs with (a) and without (b) HATCN in the charge recombination layer (CRL) under the illumination and open-circuit conditions. V_{OC1} and V_{OC2} represent the open-circuit voltages of bottom and top subcells, respectively. V_{CRL1} and V_{CRL2} are defined as the CRL-induced voltage loss. V_{OCA} and V_{OCB} are the overall open-circuit voltages of tandem OSCs with different CRLs. Dotted lines represent the quasi-Fermi-levels.

via in situ photoemission spectroscopy. It is revealed that the HATCN interlayer markedly recomposes the energy-level alignment of the interconnector with a dramatic decrease in the reverse built-in potential for electrons and holes from stacked subcells, which is profitable for the charge recombination process at the interface. In accordance with the energy-level alignments, the open-circuit voltage of a tandem OSC incorporating a HATCN-based interconnector is almost 2 times that of a single-cell OSC, revealing the effectiveness of the HATCN-based interconnectors in tandem organic devices. Moreover, the HATCN-based interconnectors can avoid the high-temperature processing, and are thus highly promising for practical applications in tandem organic solar cells.

■ ASSOCIATED CONTENT

Ⓢ Supporting Information

Additional figures showing the UPS and XPS results for the 10 nm thick CsF:BPhen (30 wt %) layer with incremental deposition of CuPc. This material is available free of charge via the Internet at http://pubs.acs.org.

■ AUTHOR INFORMATION

Corresponding Authors

*J.-X. Tang. E-mail: jxtang@suda.edu.cn.
*S. Duhm. E-mail: duhm@suda.edu.cn.

Author Contributions

The paper was written through contributions of all authors. All authors have given approval to the final version of the paper.

Notes

The authors declare no competing financial interest.

■ ACKNOWLEDGMENTS

This work is financially supported by the National Basic Research Program of China (973 Program, Nos. 2014CB932600 and 2013CB933500), the National Natural Science Foundation of China (Nos. 91027041, 61107022), Jiangsu Science and Technology Department (No. BK20140053), Jiangsu Key Laboratory for Carbon-Based Functional Materials & Devices, Collaborative Innovation Center of Suzhou Nano Science and Technology, and PAPD.

■ REFERENCES

(1) Yang, F.; Shtein, M.; Forrest, S. R. Controlled Growth of a Molecular Bulk Heterojunction Photovoltaic Cell. *Nat. Mater.* **2004**, *4*, 37−41.
(2) Kim, J. Y.; Lee, K.; Coates, N. E.; Moses, D.; Nguyen, T. Q.; Dante, M.; Heeger, A. J. Efficient Tandem Polymer Solar Cells Fabricated by All-Solution Processing. *Science* **2007**, *317*, 222−225.
(3) Li, G.; Zhu, R.; Yang, Y. Polymer Solar Cells. *Nat. Photonics* **2012**, *6*, 153−161.
(4) He, Z.; Zhong, C.; Su, S.; Xu, M.; Wu, H.; Cao, Y. Enhanced Power-Conversion Efficiency in Polymer Solar Cells Using an Inverted Device Structure. *Nat. Photonics* **2012**, *6*, 591−595.
(5) Su, Y.-H.; Ke, Y.-F.; Cai, S.-L.; Yao, Q.-Y. Surface Plasmon Resonance of Layer-by-Layer Gold Nanoparticles Induced Photoelectric Current in Environmentally-Friendly Plasmon-Sensitized Solar Cell. *Light: Sci. Appl.* **2012**, *1*, e14.
(6) Wang, P.; Wang, Y.; Tong, L. Functionalized Polymer Nanofibers: A Versatile Platform for Manipulating Light at the Nanoscale. *Light: Sci. Appl.* **2013**, *2*, e102.
(7) Liu, Y.; Yang, Y. M.; Chen, C. C.; Chen, Q.; Dou, L.; Hong, Z.; Li, G.; Yang, Y. Solution-Processed Small Molecules Using Different Electron Linkers for High-Performance Solar Cells. *Adv. Mater.* **2013**, *25*, 4657−4662.
(8) Zhou, Y.; Taima, T.; Kuwabara, T.; Takahashi, K. Efficient Small-Molecule Photovoltaic Cells Using a Crystalline Diindenoperylene Film as a Nanostructured Template. *Adv. Mater.* **2013**, *25*, 6069−6075.
(9) Pudasaini, P. R.; Ruiz-Zepeda, F.; Sharma, M.; Elam, D.; Ponce, A.; Ayon, A. A. High Efficiency Hybrid Silicon Nanopillar-Polymer Solar Cells. *ACS Appl. Mater. Interfaces* **2013**, *5*, 9620−9627.
(10) Liu, D.; Kelly, T. L. Perovskite Solar Cells with a Planar Heterojunction Structure Prepared Using Room-Temperature Solution Processing Techniques. *Nat. Photonics* **2013**, *8*, 133−138.
(11) Shockley, W.; Queisser, H. J. Detailed Balance Limit of Efficiency of p-n Junction Solar Cells. *J. Appl. Phys.* **1961**, *32*, 510−519.
(12) Hiramoto, M.; Suezaki, M.; Yokoyama, M. Effect of Thin Gold Interstitial-Layer on the Photovoltaic Properties of Tandem Organic Solar Cell. *Chem. Lett.* **1990**, 327−330.
(13) Rand, B. P.; Genoe, J.; Heremans, P.; Poortmans, J. Solar Cells Utilizing Small Molecular Weight Organic Semiconductors. *Prog. Photovoltaics* **2007**, *15*, 659−676.
(14) You, J.; Dou, L.; Yoshimura, K.; Kato, T.; Ohya, K.; Moriarty, T.; Emery, K.; Chen, C. C.; Gao, J.; Li, G.; Yang, Y. A Polymer Tandem Solar Cell with 10.6% Power Conversion Efficiency. *Nat. Commun.* **2013**, *4*, 1446.
(15) Peumans, P.; Yakimov, A.; Forrest, S. R. Small Molecular Weight Organic Thin-Film Photodetectors and Solar Cells. *J. Appl. Phys.* **2003**, *93*, 3693−3723.
(16) Riede, M.; Uhrich, C.; Widmer, J.; Timmreck, R.; Wynands, D.; Schwartz, G.; Gnehr, W.-M.; Hildebrandt, D.; Weiss, A.; Hwang, J.; Sundarraj, S.; Erk, P.; Pfeiffer, M.; Leo, K. Efficient Organic Tandem Solar Cells Based on Small Molecules. *Adv. Funct. Mater.* **2011**, *21*, 3019−3028.
(17) Dennler, G.; Scharber, M. C.; Ameri, T.; Denk, P.; Forberich, K.; Waldauf, C.; Brabec, C. J. Design Rules for Donors in Bulk-Heterojunction Tandem Solar Cells-Towards 15% Energy-Conversion Efficiency. *Adv. Mater.* **2008**, *20*, 579−583.
(18) Sista, S.; Park, M. H.; Hong, Z.; Wu, Y.; Hou, J.; Kwan, W. L.; Li, G.; Yang, Y. Highly Efficient Tandem Polymer Photovoltaic cells. *Adv. Mater.* **2010**, *22*, 380−383.
(19) Gilot, J.; Wienk, M. M.; Janssen, R. A. Optimizing Polymer Tandem Solar Cells. *Adv. Mater.* **2010**, *22*, E67−E71.
(20) Ameri, T.; Li, N.; Brabec, C. J. Highly Efficient Organic Tandem Solar Cells: A Follow up Review. *Energy Environ. Sci.* **2013**, *6*, 2390−2413.

(21) Hadipour, A.; de Boer, B.; Blom, P. W. M. Organic Tandem and Multi-Junction Solar Cells. *Adv. Funct. Mater.* **2008**, *18*, 169−181.
(22) Sun, X. W.; Zhao, D. W.; Ke, L.; Kyaw, A. K. K.; Lo, G. Q.; Kwong, D. L. Inverted Tandem Organic Solar Cells with a MoO_3/Ag/Al/Ca Intermediate Layer. *Appl. Phys. Lett.* **2010**, *97*, 053303.
(23) Timmreck, R.; Olthof, S.; Leo, K.; Riede, M. K. Highly Doped Layers as Efficient Electron−Hole Recombination Contacts for Tandem Organic Solar Cells. *J. Appl. Phys.* **2010**, *108*, 033108.
(24) Janssen, A. G. F.; Riedl, T.; Hamwi, S.; Johannes, H. H.; Kowalsky, W. Highly Efficient Organic Tandem Solar Cells Using an Improved Connecting Architecture. *Appl. Phys. Lett.* **2007**, *91*, 073519.
(25) Li, J.; Bao, Q. Y.; Wei, H.-X.; Xu, Z. Q.; Yang, J.-P.; Li, Y. Q.; Lee, S. T.; Tang, J. X. Role of Transition Metal Oxides in the Charge Recombination Layer Used in Tandem Organic Photovoltaic Cells. *J. Mater. Chem.* **2012**, *22*, 6285−6290.
(26) Meyer, J.; Hamwi, S.; Kroger, M.; Kowalsky, W.; Riedl, T.; Kahn, A. Transition Metal Oxides For Organic Electronics: Energetics, Device Physics and Applications. *Adv. Mater.* **2012**, *24*, 5408−5427.
(27) Rademacher, J. T.; Kanakarajan, K.; Czarnik, A. W. Improve Synthesis of 1,4,5,8,9,12-Hexaazatriphenylenehexacarboxylic Acid. *Synthesis* **1994**, *4*, 378−380.
(28) Niederhausen, J.; Amsalem, P.; Frisch, J.; Wilke, A.; Vollmer, A.; Rieger, R.; Müllen, K.; Rabe, J. P.; Koch, N. Tuning Hole-Injection Barriers at Organic/Metal Interfaces Exploiting the Orientation of a Molecular Acceptor Interlayer. *Phys. Rev. B* **2011**, *84*, 165302.
(29) Park, S. M.; Kim, Y. H.; Yi, Y.; Oh, H.-Y.; Won Kim, J. Insertion of an Organic Interlayer for Hole Current Enhancement in Inverted Organic Light Emitting Devices. *Appl. Phys. Lett.* **2010**, *97*, 063308.
(30) Kim, Y.-K.; Won Kim, J.; Park, Y. Energy Level Alignment at a Charge Generation Interface between 4,4′-bis(N-phenyl-1-naphthylamino)biphenyl and 1,4,5,8,9,11-Hexaazatriphenylene-hexacarbonitrile. *Appl. Phys. Lett.* **2009**, *94*, 063305.
(31) Liao, L. S.; Slusarek, W. K.; Hatwar, T. K.; Ricks, M. L.; Comfort, D. L. Tandem Organic Light-Emitting Diode Using Hexaazatriphenylene Hexacarbonitrile in the Intermediate Connector. *Adv. Mater.* **2008**, *20*, 324−329.
(32) Lin, H.-W.; Lin, W.-C.; Chang, J.-H.; Wu, C.-I. Solution-Processed Hexaazatriphenylene Hexacarbonitrile as a Universal Hole-Injection Layer for Organic Light-Emitting Diodes. *Org. Electron.* **2013**, *14*, 1204−1210.
(33) Zhang, M.; Wang, H.; Tang, C. W. Tandem Photovoltaic Cells Based on Low-Concentration Donor Doped C_{60}. *Org. Electron.* **2012**, *13*, 249−251.
(34) Xue, J.; Uchida, S.; Rand, B. P.; Forrest, S. R. Asymmetric Tandem Organic Photovoltaic Cells with Hybrid Planar-Mixed Molecular Heterojunctions. *Appl. Phys. Lett.* **2004**, *85*, 5757−5759.
(35) Peisert, H.; Knupfer, M.; Schwieger, T.; Auerhammer, J. M.; Golden, M. S.; Fink, J. Full Characterization of the Interface between the Organic Semiconductor Copper Phthalocyanine and Gold. *J. Appl. Phys.* **2002**, *91*, 4872−4878.
(36) Lee, S.; Lee, J.-H.; Kim, K. H.; Yoo, S.-J.; Kim, T. G.; Kim, J. W.; Kim, J.-J. Determination of the Interface Energy Level Alignment of a Doped Organic Hetero-junction Using Capacitance−Voltage Measurements. *Org. Electron.* **2012**, *13*, 2346−2351.
(37) Hill, I. G.; Kahn, A.; Soos, Z. G.; A, P. R., Jr. Charge-Separation Energy in Films of p-Conjugated Organic Molecules. *Chem. Phys. Lett.* **2000**, *327*, 181−188.
(38) Meyer, J.; Kröger, M.; Hamwi, S.; Gnam, F.; Riedl, T.; Kowalsky, W.; Kahn, A. Charge Generation Layers Comprising Transition Metal-Oxide/Organic Interfaces: Electronic Structure and Charge Generation Mechanism. *Appl. Phys. Lett.* **2010**, *96*, 193302.
(39) Oehzelt, M.; Koch, N.; Heimel, G. Organic Semiconductor Density of States Controls the Energy Level Alignment at Electrode Interfaces. *Nat. Commun.* **2014**, *5*, 4174.
(40) Braun, S.; Salaneck, W. R.; Fahlman, M. Energy-Level Alignment at Organic/Metal and Organic/Organic Interfaces. *Adv. Mater.* **2009**, *21*, 1450−1472.
(41) Ishii, H.; Hayashi, N.; Ito, E.; Washizu, Y.; Sugi, K.; Kimura, Y.; Niwano, M.; Ouchi, Y.; Seki, K. Kelvin Probe Study of Band Bending at Organic Semiconductor/Metal Interfaces: Examination of Fermi Level Alignment. *Phys. Status Solidi A* **2004**, *201*, 1075−1094.
(42) Lee, S.; Lee, J.-H.; Lee, J.-H.; Kim, J.-J. The Mechanism of Charge Generation in Charge-Generation Units Composed of p-Doped Hole-Transporting Layer/HATCN/n-Doped Electron-Transporting Layers. *Adv. Funct. Mater.* **2012**, *22*, 855−860.
(43) Yu, B.; Zhu, F.; Wang, H.; Li, G.; Yan, D. All-Organic Tunnel Junctions as Connecting Units in Tandem Organic Solar Cell. *J. Appl. Phys.* **2008**, *104*, 114503.